



# Electron beam powder bed fusion of Ti-6Al-2Sn-4Zr-2Mo lattice structures: morphometrical and mechanical characterisations

Manuela Galati<sup>1</sup> · Massimo Giordano<sup>1</sup> · Abdollah Saboori<sup>1</sup> · Silvio Defanti<sup>2</sup>

Received: 16 November 2023 / Accepted: 28 January 2024 / Published online: 5 February 2024  
© The Author(s) 2024

## Abstract

Metallic light and complex structures, such as lattice, made by Ti-6Al-2Sn-4Zr-2Mo (Ti6242) have potential applications in many different industries, especially in light and high-temperature-resistant aerospace and aeronautical components. An advantage of the electron beam powder bed fusion (PBF-EB) process over conventional and other additive manufacturing processes is the ability to fabricate lattice structures easily. However, the control of the effect of the manufacturing process for fabricating such small features is central to define the structure's mechanical properties. This work investigates the effects of PBF-EB parameters on the geometrical quality of Ti6242 lattice structures. The selected cell consists of 12 rhombic areas connected by 24 struts joined in 12 vertices. The structures were produced in two cell sizes and two strut diameters under nine different process sets. X-ray computed tomography and scanning electron microscopy analyses were used to characterise the morphometrical parameters of each as-built cell and the interlayer integrity of the struts. Evolution under compressive loads was used to determine the mechanical properties of the lattice structures and the failure mechanism underlying the influence of process parameters on the mechanical properties. The as-built Ti6242 lattices were well-formed without voids and cracks. The outcomes revealed a significant effect of the considered lattice structure and process setup on the morphometric parameters. Even minor variations of the main processing parameters considerably impacted the mechanical properties of the structure.

**Keywords** Lattice structures · Electron beam melting · Ti-6Al-2Sn-4Zr-2Mo · Titanium alloys · Additive manufacturing · CT scan

## 1 Introduction

Additive manufacturing (AM) unlocked several design opportunities, including producing unfeasible structures with conventional manufacturing processes. Representative of such potential is the reticular structures, also called lattices [1]. This architected structure consists of an ordered repetition of an elementary cell in the 3D space [2]. The elementary cell may be composed of struts, usually cylindrical beams, arranged in the space and jointed in specific

nodes [3]. The morphometric parameters that describe the structure are the cell topology, the cell size, and the strut diameter [4]. The combination of such parameters defines the relative density of the structure that represents the actual volume of material compared with the overall dimensions of the structure. The relative density is, therefore, a descriptor of the porosities in the lattice [5–9]. All these geometrical parameters, together with the material and its structural integrity, define the mechanical performances of the structure [4, 10]. Because of the architectural complexity, manufacturing lattice structures also requires attention in AM. Depending on the morphometric parameters of the structure, the fabrication may be unfeasible because of the need to use support structures that, for thin reticular geometries, would be impossible to remove [11]. In the case of metallic components, processes such as electron beam powder bed fusion (PBF-EB/M) are preferable to produce lattice constructs because the sintered powder bed is strong enough to avoid the use of support structures [12]. Moreover, this AM

✉ Manuela Galati  
manuela.galati@polito.it

<sup>1</sup> Integrated Additive Manufacturing Center (IAM),  
Department of Management and Production Engineering  
(DIGEP), Politecnico di Torino, Corso Duca degli Abruzzi,  
24 Torino, Italy

<sup>2</sup> Department of Engineering “Enzo Ferrari,” Università Degli  
Studi di Modena e Reggio Emilia, Modena, Italy

technology features a vacuum environment in the production phase which is a significant advantage to processing sensible oxygen alloys [13]. Among the materials, the most used is Ti6Al4V (Ti64). However, this material has some limitation regarding to high-temperature applications, harsh corrosive environments, and, for biomedical implant, the presence of Vanadium and its oxide which may cause allergic and inflammatory reactions [14]. On this regard, the number of materials for PBF-EB/M is rapidly increasing, especially in the field of titanium alloys. Recently, Ti-6Al-2Sn-4Zr-2Mo (Ti6242), a near  $\alpha$ -alloy [15], has been optimised for producing bulky components [16]. The mechanical properties of bulky components produced PBF-EB/M were comparable to the corresponding casted material [16]. However, creating thin features such as beam reticula requires specific process optimisation [4] and has never been investigated for Ti6242.

This work investigates the PBF-EB/M process for producing Ti6242 lattice structures. In particular, the effect of various processing conditions on the geometrical quality of the structure are analysed by X-ray computed tomography (CT) and scanning electron microscopy analyses. Each structure is examined considering the interlayer integrity of the struts and the comparison between the nominal and the actual morphometrical parameters of the cell. The samples are tested under uniaxial compression, and the mechanisms underlying the influence of process parameters on the mechanical properties of the sample are analysed.

## 2 Materials and methods

### 2.1 Design of experiment and production

The cell selected for the study consists of 12 rhombic areas connected by 24 struts joined in 12 vertices (Fig. 1). This cell, called dodecahedron (dode), is one of the most used in the literature [3, 9, 17, 18] and was selected within the database available on Materialise Magics, which also integrates the build processor for the PBF-EB/M system. The cell can

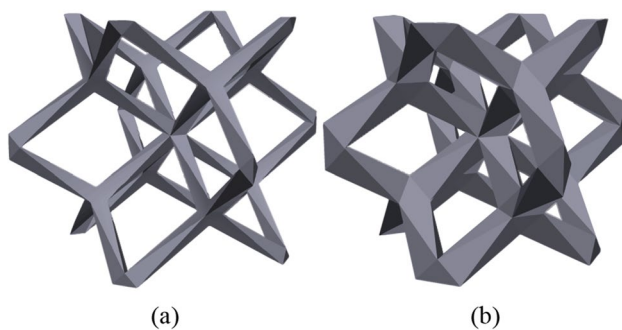


**Fig. 1** Dodecahedron unit cell: strut size **a** thin and **b** medium

be designed with different strut sizes, which, on equal cell size, correspond to different relative densities. In this case, the thin series (T series, Fig. 1a) and the medium one (M series, Fig. 1b). The corresponding strut size depends on the cell size, and it is adapted to keep constant the ratio between the strut length and diameter and provide a certain stiffness for larger cell under load. In this work, two different cell sizes are analysed, 3 mm and 5 mm.

Table 1 shows the nominal morphometrical parameters of each elementary cell.

The sample for the mechanical test was a cube with a 20-mm edge where the unit cell was orderly repeated.

Concerning the production, owing to such small features' dimensions compared with the electron beam diameter [13], material melting was performed using a contour strategy, often called contouring. The contours can be distinguished into outer (out) and inner (in) contours (Fig. 2).

The PBF-EB systems operate with constant acceleration voltage. Therefore, the process parameters for melting each contour that define the quality of the structure are the scan speed ( $v$ ), the beam focus offset (FO), and the beam current ( $I$ ). The combination of scan speed, beam current, and acceleration voltage defines the energy the electron beam provides to melt the metallic powder particles. The spot size is controlled jointly by the focus offset and the beam current [4, 20] and defines the dimension of the area in which the beam energy is distributed. The spot size is not user-controllable.

**Table 1** Nominal morphometric properties of each structure. The nominal size varies proportional to the cell size

ID	Series	Cell dimension (mm)	Nominal strut dimension (mm)	Nominal relative density (-)
M3	M	3	0.41	12.62%
M5	M	5	0.68	12.47%
T3	T	3	0.22	3.93%
T5	T	5	0.37	3.89%

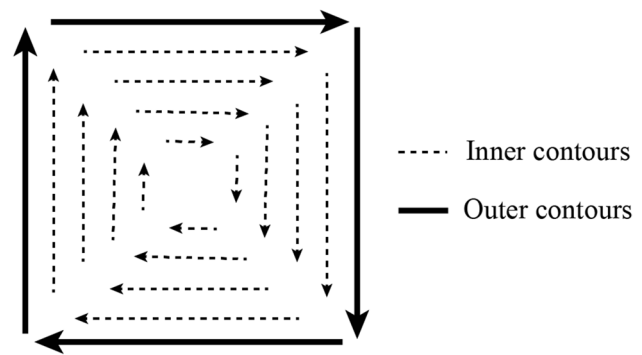


**Fig. 2** Contouring scanning strategy [19]

The PBF-EB/M system adopted for the production was an Arcam A2X, which operates at a constant acceleration voltage of 60 kV. The layer thickness was set at 50  $\mu\text{m}$  [16]. The preheating parameters were extracted from Ref. [16]. The parameters for the melting were varied according to Table 2. Each combination of process parameters was named NET followed by a progressive number. The values were kept in small range of variation to observe the sensitivity of the structure morphometry and the mechanical properties. The increasing of the beam current level at the outer contour (NET2 vs NET4) and at the inner contour (NET4 vs NET5) is expected to produce thicker struts due to the increased energy density. The variation of the scan speed level (NET1 vs NET2 vs NET7) causes a variation in the beam resident time during the melting phase. Within certain limits, a faster beam is expected to produce a slimmer melting line. The focus offset variation at the outer contour modifies the beam diameter, thus affecting the accuracy of the melted geometry (NET5 vs NET6 or NET1 vs NET9).

All samples were produced on a stainless-steel start plate (210 mm  $\times$  210 mm  $\times$  10 mm) in a single job (Fig. 3). Each cubic specimen was tilted by 45 degrees with respect to the

build platform to avoid the use of support structures (Fig. 3). To prevent any thermal effect that might influence the geometrical quality, the samples were produced at 5 mm from the start plate and equally spaced among each other. The arrangement of samples on the platform is shown in Fig. 3, where the colour indicates the nominal geometrical features (Table 1), and the numeric label indicates the corresponding NET (Table 2). The NETs were spatially randomised to avoid any location-dependent influence.

At the end of the production, the job was cooled down in the machine chamber using a helium flow. The samples were then shot blasted at 4.5 bar, with the same raw powder used for the construction.

Ti–6Al–2Sn–4Zr–2Mo alloy powder supplied by TLS Technik GmbH & Co. with particle size between 45  $\mu\text{m}$  and 106  $\mu\text{m}$  and a median volume diameter of approximately 75  $\mu\text{m}$  was used as material for the production [16].

### 2.2 Geometrical characterisation

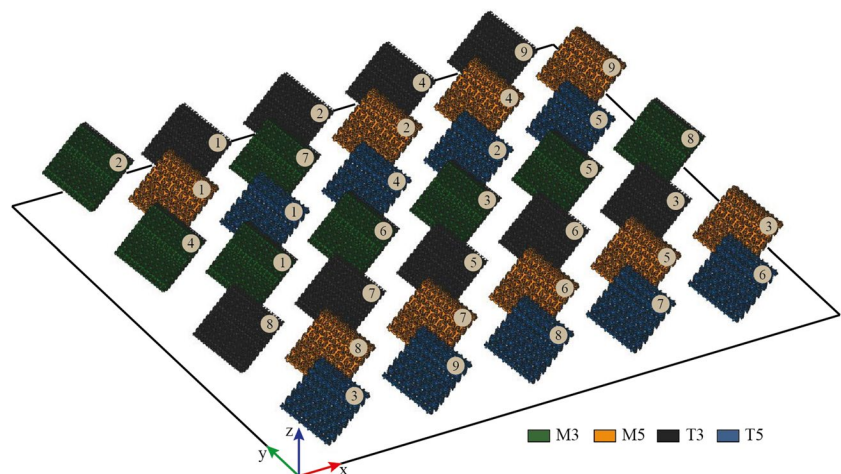
The integrity of the samples at the micro-scale and the presence of inaccuracies or defects were checked through observations using a calibrated stereomicroscope Nikon Eclipse LV150N (Nikon, Tokyo, Japan) and a scanning electron microscope ESEM Quanta 200 (FEI Company, Bruker corporation, Hillsboro, Oregon, USA).

Each sample was also scanned using an X-Ray CT scanner (GE Phoenix v tomelx s). The scans were executed using a voltage of 240 kV, a current of 110  $\mu\text{A}$  and a 0.5-mm Sn with an additional 0.1-mm-thick Cu filter. 1001 2D projections were collected for each sample. The voxel size was set to 0.030 mm, comparable to half of the layer thickness and smaller than the particle size. The post-processed reconstructed CT projections were investigated using VGStudio-Max 3.4. The morphometrical parameters extracted for the analysis were the strut diameter, the relative density of the structure and the cross-section. The morphometric analyses

**Table 2** DOE according to the process parameter combinations

NET	$v_{out}$ (mm/s)	$I_{out}$ (mA)	$v_{in}$ (mm/s)	$I_{in}$ (mA)	$FO_{out}$ (mA)
1	450	2.8	470	2.4	0
2	490	2.8	470	2.4	0
3	450	2.8	500	2.4	0
4	490	3.2	470	2.4	0
5	490	3.2	470	3.2	0
6	490	3.2	470	3.2	5
7	520	2.8	470	2.4	0
8	450	2.8	520	2.4	0
9	450	2.8	470	2.4	5

**Fig. 3** Job configuration. Numeric labels refer to the cell geometry in Table 1 and the combination of process parameters (NET) in Table 2. The z-axis corresponds to the build direction



were conducted on a portion of the scanned structure called “region of interest (ROI)”. The “wall thickness analysis” (WTA) tool was applied to measure the strut average dimension automatically and performed using the sphere method. The output is an occurrence histogram providing the mean measurement of the strut with the corresponding deviation. Some correction was applied to the output values: the smallest and largest values were excluded from the calculation because they referred to the ROI border and the connection nodes of the struts, respectively. The mean has been calculated from over one million measurements.

For example, considering the same cell geometry M5, WTA showed a significant effect of processing parameters setting (Fig. 4). It can be noticed that the cell M5 melted with NET 9 (Fig. 4b) consists of slimmer struts than the corresponding sample melted using NET 3 (Fig. 4c). In this case, the cell M5 melted using NET 2 (Fig. 4b) showed the largest presence of surface irregularities with features thinner than 0.5 mm. On the other hand, the cell M5 melted using NET 3 (Fig. 4c) showed the largest nodes.

In the second step, randomly located struts were measured with the cylindrical approximation tool to derive the mean strut diameter and to establish the sensitivity of the WTA tool to surface defects on the struts. A comparison between the two methods is reported in Fig. 5. The cylindrical approximation provides the fitting with the considered geometry and the point-by-point deviation (Fig. 5a), which accounts for the local process-induced irregularities at different sections, as also observed in Ref. [21]. Focusing on a single strut, the mean diameter obtained from the WTA differs from the cylinder fittings because it considers all the irregularities on the external surface as diameter measurements (Fig. 5b), affecting the mean value. The cylinder

fitting measurements overcome this limitation since the gauges are always included within the deviation of the WTA.

The effective relative density, measured as the ratio between the material volume and the isolated ROI volume, was estimated on a large portion of the specimen, including multiple elementary unit cells (an example is provided in Fig. 6).

The minimum section was selected at a nodal plane and was measured from the CT-extracted cross-sections (see, e.g., Fig. 7). The stress-bearing area and the dimensions of the specimens were computed with image analysis software (ImageJ).

### 2.3 Mechanical characterisation

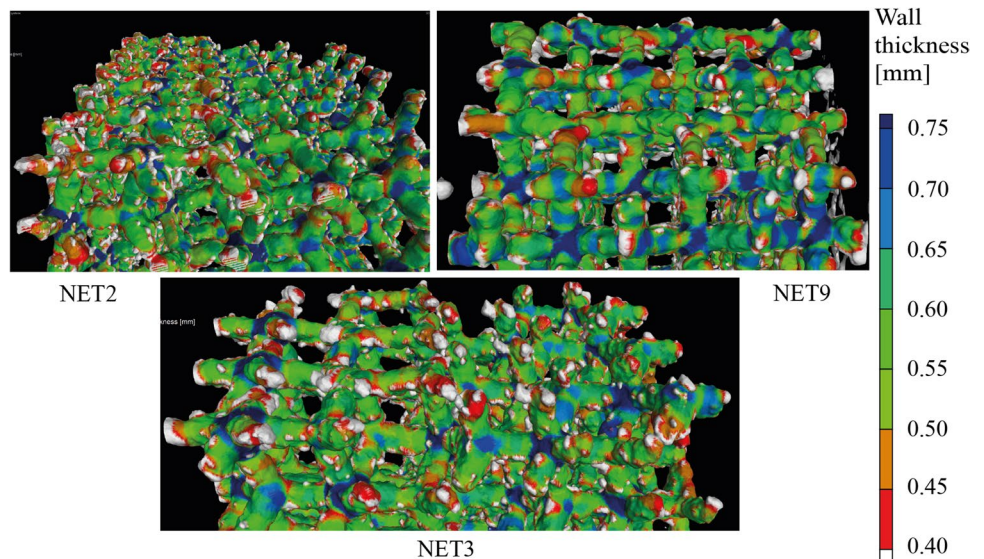
Each sample was tested under uniaxial compression using an AURA 10 TIEASYDUR ITALIANA with 100 kN maximum load capacity. During the test, the compression speed was set at 1.5 mm/min and was applied up to the total collapse of the structure. The load/displacement data were collected with a 500 Hz sampling frequency.

Using an analytical approach, the data post-processing to derive the stress/strain curves were based on the linear elastic law.

$$\sigma = E \cdot \varepsilon$$

where  $\sigma$  is the stress expressed in MPa and equal to the ratio between the load,  $L$ , and the cross-section,  $A_0$ , obtained as reported above;  $\varepsilon$  is the strain and is equal to the ratio between the deformation of the sample ( $l-l_0$ ) and the initial length of the sample,  $l_0$ . Young’s modulus ( $E$ ) was obtained by linear interpolation of the stress-strain curve in the elastic region.

**Fig. 4** Wall thickness analysis applied to M5 specimens produced under different processing conditions



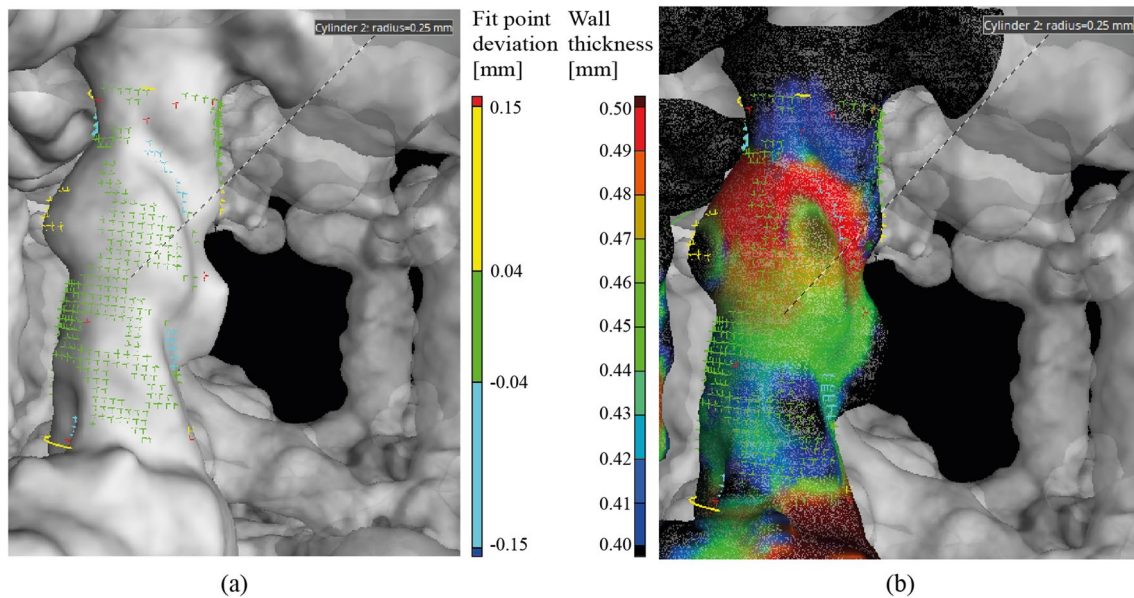


**Fig. 5** **a** Cylinder approximation and **b** WTA approach applied to a single strut of the T5 produced with NET8

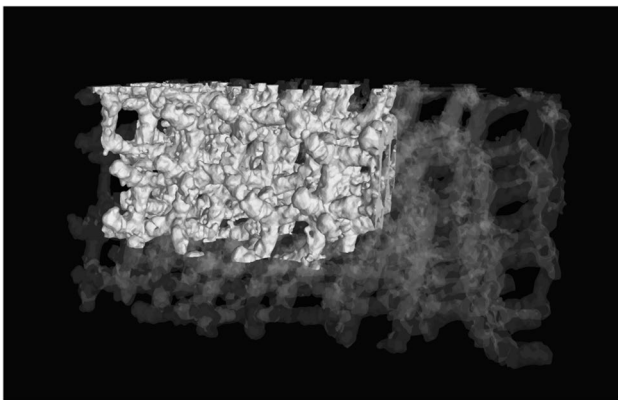


**Fig. 6** Effective relative density estimation in a ROI

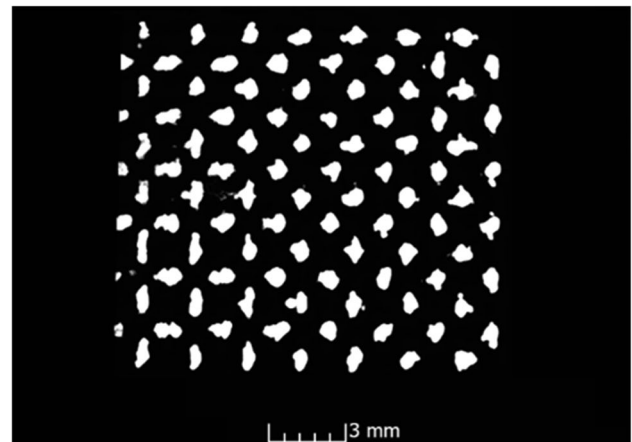


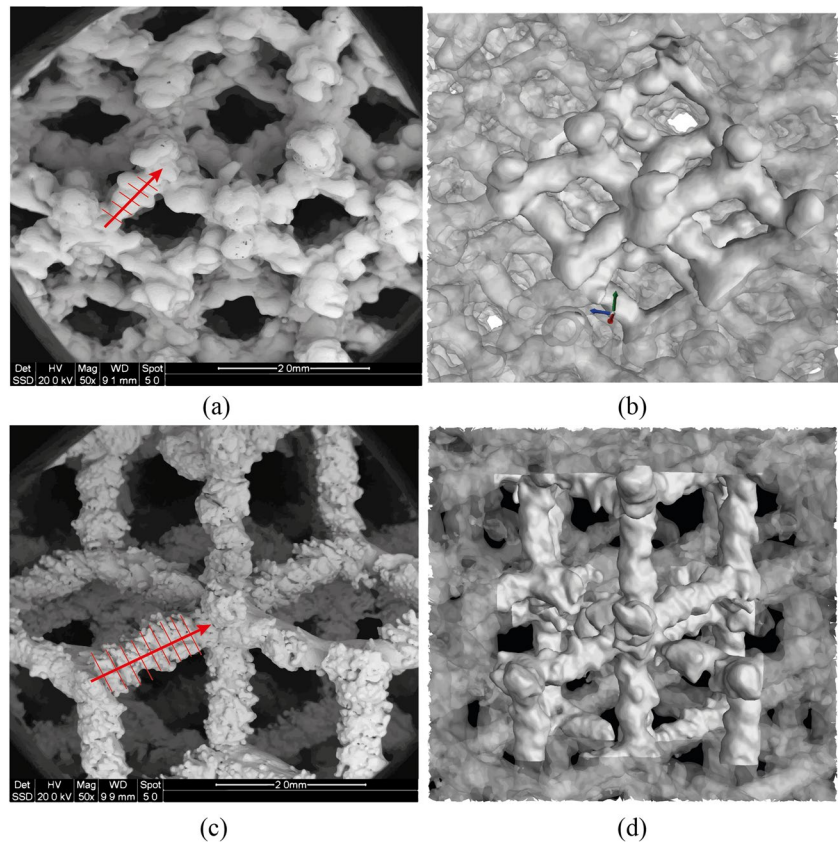
**Fig. 7** Example of a node cross-section for the extraction of the stress-bearing section

### 3 Results and discussion

All the as-built Ti6242 lattices were well-formed. For example, Fig. 8 compares SEM and CT scan images of the geometry of the cells T3 and T5, respectively, produced using NET8. Both measuring systems could detect the irregularity of the struts. The struts detected by X-Ray CT analyses appear smoother because the resolution did not detect the actual surface morphology generated by the melting or the particles attached to the strut surface. SEM images (Fig. 8a, c) show that the same process parameter setting produced significantly different morphologies when referred to different cell dimensions. In particular, the T3 cell appears less defined than the corresponding T5. It seems that the

struts of the T3 cell are overmelted, creating some irregular bumps, without particles attached to the surfaces. The shape of T5 cells is more defined and well-recognisable. As typical for PBF-EB/M processes, the surfaces are characterised by satellite particles [22]. Also, a presumable layerisation is visible in the direction indicated by the red arrow in Fig. 8. The differences observed by the melting of different struts with the same processing parameters may depend on the nominal dimensions of the struts. The nominal size of the T3 struts may be too thin to be properly melted by NET8, thus being below the manufacturing capability for that process configuration.

**Fig. 8** Portions of T3 (a, b) and T5 (c, d) specimens fabricated with NET 8. SEM images (a, c) and CT scan reconstructions (b, d). The red arrow indicates the build direction and the layerisation effect



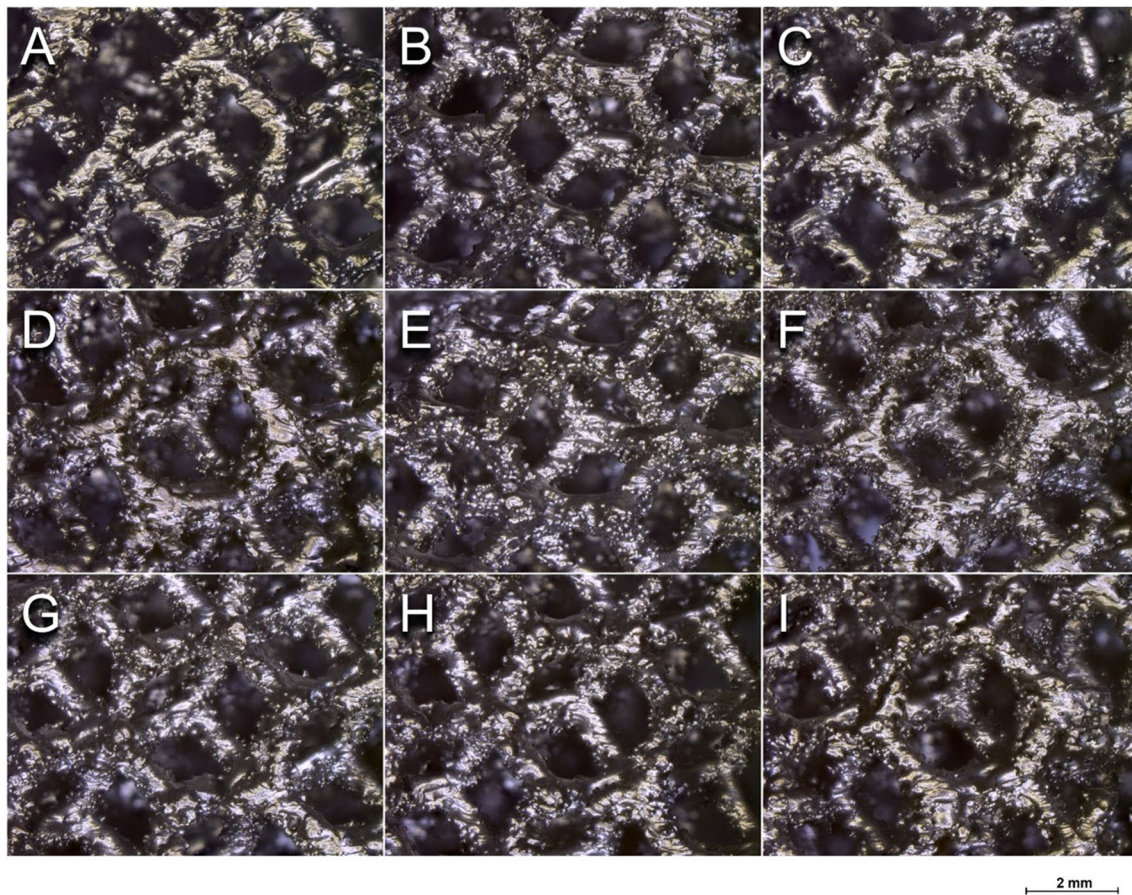
An overall view of the accuracy of M5 structures produced with the varying process setups is offered in the collection of optical images in Fig. 9. More details can be appreciated in the SEM images in Fig. 10, where one complete cell for each structure is shown on the side of the upskin surface [22]. Fig. 11 displays magnified views of a single diagonal strut for each NET condition. The images allow to verify the amount of satellite particles that remain attached to or partially melted into the downskin region of the strut. This additional material represents an extra mass with respect to the nominal density of the lattice reticulum [23] but rarely contributes to the mechanical response [24]. Cracks are sporadically observed, among many other sources of unevenness, such as the staircase effect, melt pool superimposition, and local strut thinning due to melt instability or shrinkage.

Fig. 12 shows the actual strut dimension and relative density for each cell and each process parameter setting, compared with the nominal values. The first observable result is that, in almost all cases, the actual strut dimension is larger than the corresponding nominal one. The result is consistent with the morphology shown in Figs. 9, 10, and 11. The smaller the nominal strut size is, the larger the deviation from the nominal value is. The maximum error between the actual and the nominal strut size can be detected for cell T3, for which the nominal strut is the lowest (Table 2). On the

contrary, the smallest deviation from the nominal dimension is for cell M5 for which the strut size is the largest (Table 2). The cells T3, T5 and M3, in which the deviation between the actual and nominal strut dimensions was above 25%, identify the technological limit of the system, which is presumably associated with the beam spot [4, 20]. It can be observed that the effect of the processing conditions depends on the cell size. For example, the processing setting from NET1 to NET5 produced systematically thicker struts in case of a cell size equal to 5 mm.

Cell T3 is the structure with nominally the smallest strut size (Table 2). This condition pushed the process close to the technological limit of the system [4] because, for all the processing conditions, the obtained strut is much thicker than the nominal one, with an almost constant error (55%) from the nominal value and a small data dispersion (Fig. 12a). The same conclusion can be drawn for the relative density of the structure, except for the combination of processing conditions NET1 and NET4. For these setups, the higher relative density values can be explained by larger nodes, as can be detected by the cross-section values (Fig. 13).

Considering the cell T5 structure (Fig. 12b), the effect of the variation of the processing condition becomes more relevant. However, even in this case, the actual strut size was always larger than the nominal one, with a maximum deviation below 40%. Therefore, the nominal dimension of



**Fig. 9** Optical images of M5 samples produced with **A** NET1, **B** NET2, **C** NET3, **D** NET4, **E** NET5, **F** NET6, **G** NET7, **H** NET8 and **I** NET9

the strut is still below the technological limit of the system. NET2, NET3, NET4 and NET5 generally produced the thickest struts. Those combinations are associated with more focused beam, lower scan speed or higher beam current that generally increase the heat provided during the melting, producing larger melt pools and, therefore, larger struts.

Slimmer struts were obtained by increasing the beam current at the inner contour (NET4 vs NET5). However, the effect on the relative density is limited because the external volume of the structure was defined by the outer contour which is melted before the inner ones. Contrasting results can be observed by varying the scan speed for the inner contours. By fixing the process parameters at the lowest levels considered in this DoE and let the scan speed vary at the inner contour (see NET1 vs NET3 vs NET8), the thickest struts are measured in correspondence with the intermediate value of  $v_{in}$  where the relative density is also the highest. Considering NET4, NET5 and NET6, the increase of beam current level at the inner contour (NET4 vs NET5) produces a smaller beam diameter. The features are even smaller when the FO at the outer contour is increased (NET5 vs NET6).

By increasing the nominal dimension of the struts, the error between the actual strut dimension and the nominal one decreases. Cell M3 shows an error ranging between 26% and 35%; therefore, the processing conditions can still be considered at the technological limit of the system. Only when the nominal strut size became around 0.7 mm, as in the case of cell M5, the errors with respect to the nominal geometry are, in several cases, null.

For M3 (Fig 12c), the increase of scan speed at the outer contour (NET 1, NET2 vs NET7) or the beam current at the outer contour (NET2 vs NET4) produced a larger mean value for the strut size. However, the dispersion of the measurements is, in certain case, large and the deviation errors bars overlap, evidence of that the difference amount the set is not probably statistically significant. Fixing the focus offset, the beam current variation significantly contributes to the strut size. In particular, when increased at the outer contour (e.g. comparing NET 2 vs NET4), it results in thicker struts. The focus offset at 5 mA, when combined with a beam current of 3.2 mA (NET6) produced slightly smaller features compared to NET5, without affecting the level of the defects.

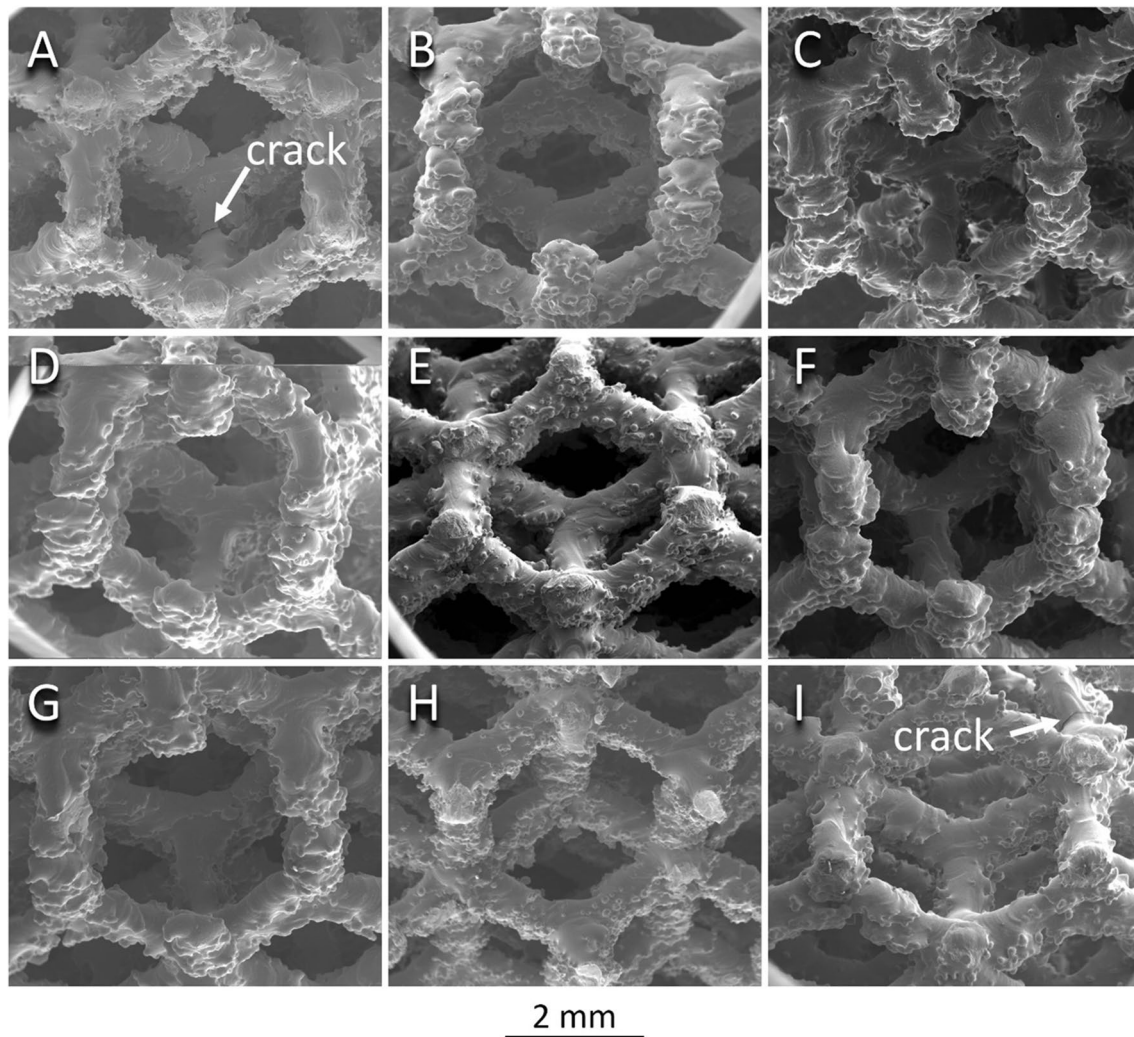


**Fig. 10** SEM images of M5 samples produced with **A** NET1, **B** NET2, **C** NET3, **D** NET4, **E** NET5, **F** NET6, **G** NET7, **H** NET8 and **I** NET9

The simultaneous increase of beam current at the inner contour and focus offset at the outer contour (NET4 vs NET6) resulted in bigger features, but slimmer than the one produced with NET5 where only the beam current is varied.

In the case of cell M5, for which the error compared to the nominal strut size is the lowest, the effect of varying the process parameters can be better highlighted. NET7 and NET9 produced a strut size comparable to the nominal one, while NET5 produced regular struts with the lowest data dispersion. This reflects the more regular struts associated with that process parameter combination. The highest deviation from the nominal dimensions has been obtained for the process setting corresponding to NET3 and NET4, which correspond to high current or high-speed values. These combinations may generate unstable process conditions, which explains the larger strut and the more pronounced standard deviation. In any case, NET3 and NET4 produced comparable strut dimensions; the average strut dimension differs

by 1.5%, with slightly thicker values associated with NET 4. The result matches well with SEM images, where the high amount of extra material is evident in Figs. 10d and 11d. This can be explained by considering that the high beam current on the outer contour and the low scan speed at the inner contour produced a larger melt pool resulting in a larger strut dimension. In general, it appeared that for low beam current values, a larger focus offset produced more regular struts with a lower standard deviation (NET1 vs NET9 or NET7 vs NET9). The opposite result was obtained when the beam current was higher (NET5 vs NET6). As mentioned in Section 2.1, the focus offset and the beam current jointly controlled the spot size [4, 20], which in turn defines the dimension of the area in which the beam energy is distributed. Since the spot size is not user-controllable and unknown, it could presume that the more defined strut is due to a lower spot size, obtained at the selected values of beam current and focus offset.



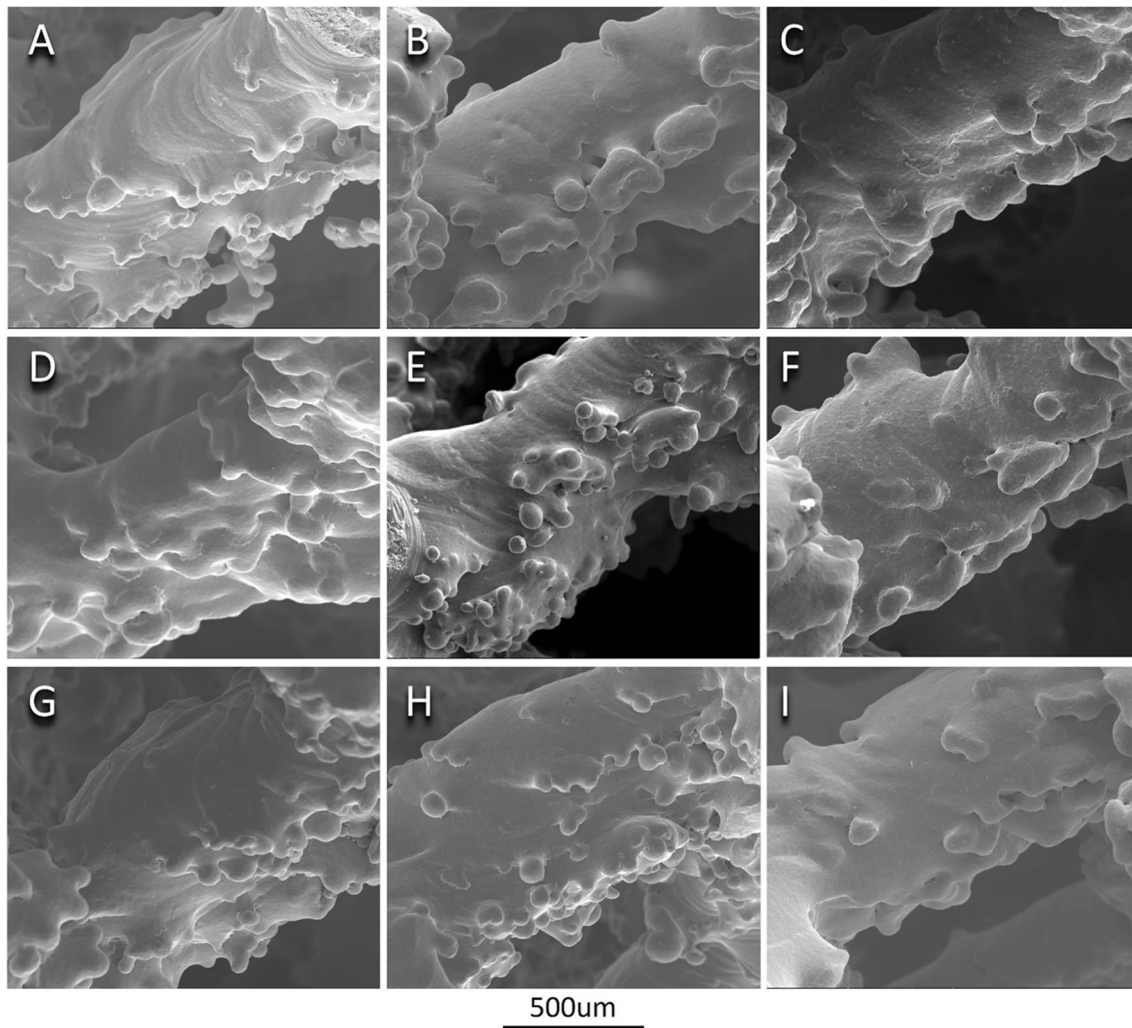


**Fig. 11** SEM images of single struts of M5 samples produced with **A** NET1, **B** NET2, **C** NET3, **D** NET4, **E** NET5, **F** NET6, **G** NET7, **H** NET8 and **I** NET9

For the same focus offset, when the beam current increases, the struts are thicker (NET6 vs NET9) and even thicker when the increase of beam current is for the outer contour (NET2 vs NET4).

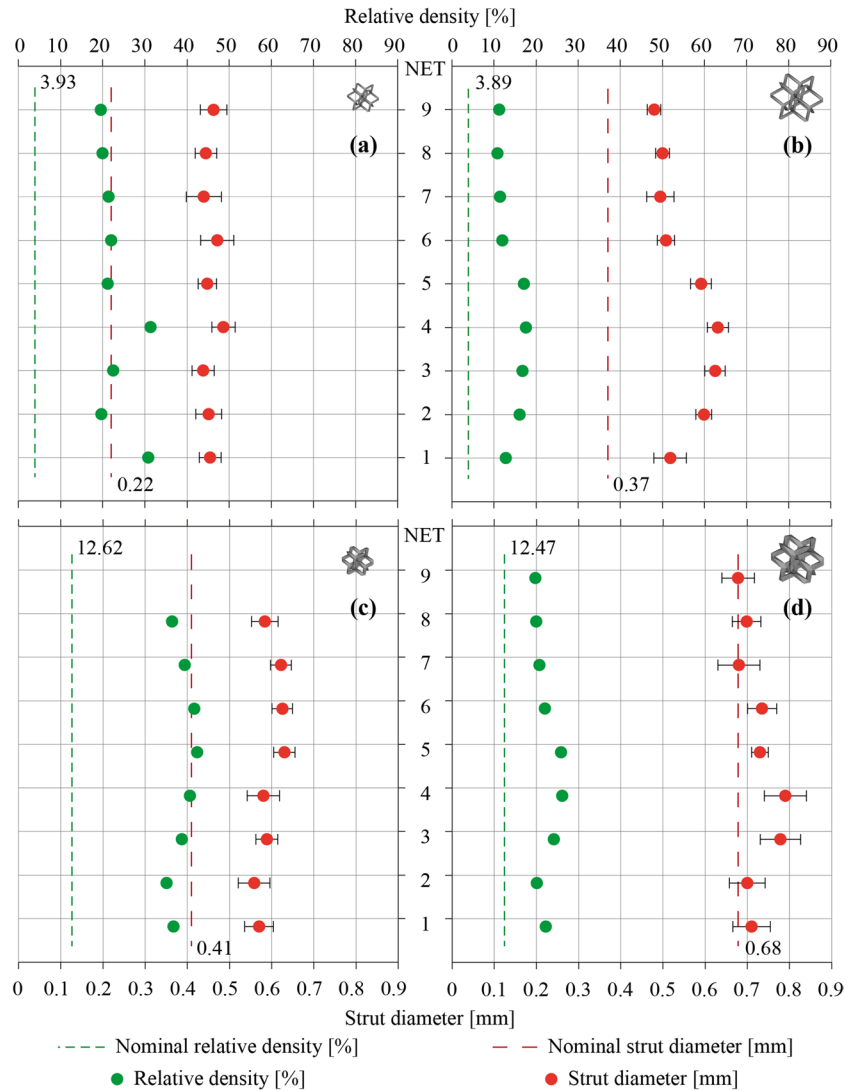
The trend for the scan speed is also confirmed in this case. When the scan speed is increased at the outer contour (e.g. NET1 vs NET2 vs NET7, NET3 vs NET8), slimmer struts are produced. This can be explained by the lower resident time for melting when the beam is faster.

In summary, the beam current at the outer contour produced systematically thicker struts in all cases because of the high beam power. On the other hand, the struts are thinner when the beam current is higher at the inner contour, except for cell M3. An equally general conclusion cannot be drawn for the scan speed levels at the inner and outer contours. This proves that such parameters are not a leading factor for determining lattice structure accuracy in the range of investigated values.

The strut size is also influenced by varying the beam current and focus offset simultaneously (e.g., NET1 vs NET9 or NET5 vs NET6). This variation presumably affects the beam diameter and, consequently, the melt pool and strut size. In addition, different combinations of those parameters might produce more irregular struts, as observed from the standard deviation associated with the mean strut measurement (e.g. T3 and M5 cells with NET5 vs NET6, T5 structure NET1 vs NET9). The measure of the deviation from the nominal design reflects the technological limit of the system on producing such small structures, independently of the process parameter set. This limit has been found to be around 0.450 mm.

The measured relative density value was always larger than for the designed structure, independent of the process parameter combinations investigated in the current work. Generally, the trend of relative density variation followed the one described for the strut dimensions. The few exceptions

**Fig. 12** Comparison between nominal and measured morphometric properties for **a** T3, **b** T5, **c** M3 and **d** M5 structures. The surface irregularities are reported in the associated interval bar as deviation



can be explained with irregular struts (large standard deviation), as in the case of cell T3 with NET6 and NET7, or with larger nodes as detected by the cross-section areas (Fig. 13) for the cell T3 produced with NET1 and NET4.

A further graphical comparison between the morphological characteristics (strut size, cross-section and relative density) and the results of the uniaxial compression tests of each single cell is shown in Fig. 13. For the sake of completeness, separated graphs for each single cell are reported in the Appendix, and the values are reported in Table 3.

Overall, the mean strut measure is characteristic of the single cell, while the same cannot be affirmed for the relative density and the cross-section. In particular, the cells M3 and T5 differ systematically from the other cells for all the processing conditions. Cell T5 showed a similar strut dimension to cell T3. However, the larger cell size (5 mm against 3 mm) led to lower cross-section and relative density values. These values are also the lowest among all the cells,

and this involves a systematic effect on the mechanical properties, which are steadily lower for every processing condition. Therefore, combining thin struts and large cell sizes involved the poorest mechanical performances. Averagely, cell M3 is the one that performed the best. This result can be explained by the robustness of the cell that showed the highest relative density and the largest cross-section for all the processing conditions. The lowest Young modulus and UCS (Uniaxial Compressive Strength) values are associated with the thinnest struts because the ratio between length and diameter became high. In this case, the strut behaves as a slender beam and is prone to bending. This peculiarity is more evident when the mechanical properties are associated with the stress-bearing section and the relative density, which present the same variation trend because of the different process parameter combinations. This effect can be observed when comparing the different structures, such as the cells T3 and M3. The strut dimensions are similar in

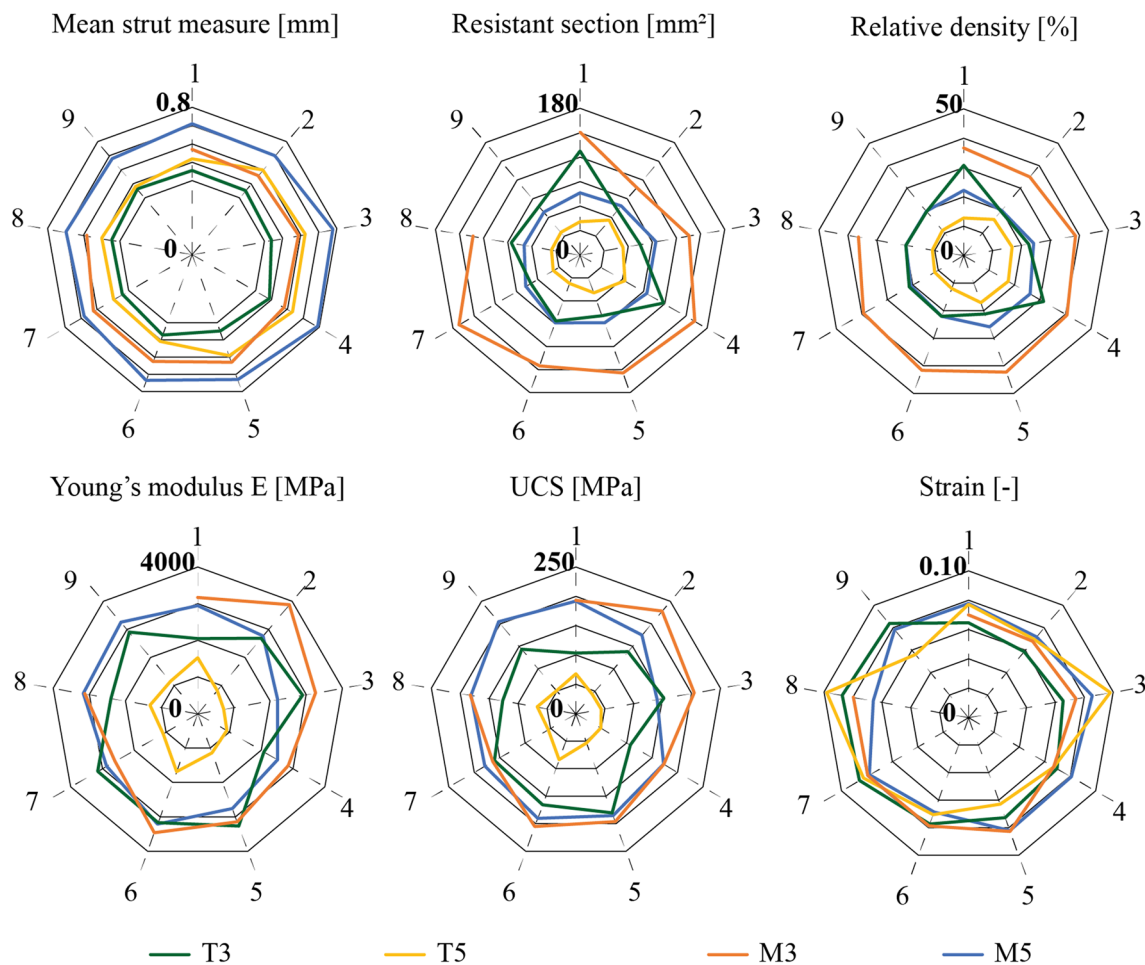


**Fig. 13** Mechanical properties of the lattice structures referred to the morphometry. The number from 1 to 9 of each radius referred to the processing condition (NET)

this case, but the mechanical properties are systematically different. The Young modulus for the cell T5 is half of the cell M3, and the UCS of T5 can be up to 75% lower than the corresponding one for M3. Consequently, the cell dimension has a remarkable influence on mechanical behaviour. This conclusion is also confirmed when comparing T3 and T5 and M3 and M5. Even if a thicker strut characterises the 5 mm unit cell, it has systematically lower mechanical properties.

Overall, the UCS value followed Young modulus variation. However, this property is less sensitive to the process parameters variation: an example is cell M5, for which a relevant difference could be detected only when the sample was produced using NET9.

Specifically observing the performances for the same cell at different process settings, it can be noticed that the highest mechanical properties can be detected when the deviation between the nominal strut value and the actual strut size is lower. For example, the values obtained for cell M5 produced with NET7, NET8 or NET9 and cell M3

manufactured using NET2 or NET3 are worth noting. This result may be explained mainly through a higher smoothness with which the electron beam melts the section.

Considering each cell, as observed for the strut size, it is possible to note that the best process parameter setting depends significantly from the nominal size of cell and the strut. Among the process parameters, a systematic difference of above 30% can be observed between the maximum and minimum values of *E* and UCS (Table 3). Specifically, the following findings can be resumed:

- Cell T3 showed the highest Young modulus when produced with the process parameter set NET5, whereas the minimum was measured when the sample was produced using NET1 and NET4, leading to the biggest cross-section and highest relative density. A similar result was obtained for the UCS values. The maximum strain value has been measured in the sample produced using NET 8.
- Cell T5 showed the highest Young modulus and UCS when produced using NET6, NET1 or NET8. The mini-

**Table 3** Mechanical properties

Cell type	Cell size (mm)	NET	E (MPa)	UCS (MPa)	Strain (-)
T	3	1	2048	103	0.06
T	3	2	2683	138	0.06
T	3	3	2900	152	0.07
T	3	4	2083	107	0.07
T	3	5	3267	180	0.07
T	3	6	3167	166	0.08
T	3	7	3149	160	0.09
T	3	8	2400	127	0.09
T	3	9	2900	143	0.08
T	5	1	1524	68	0.08
T	5	2	825	43	0.07
T	5	3	716	44	0.10
T	5	4	916	49	0.07
T	5	5	1141	53	0.06
T	5	6	1686	84	0.07
T	5	7	1091	55	0.08
T	5	8	1321	67	0.10
T	5	9	1152	51	0.06
M	3	1	3167	193	0.07
M	3	2	3881	228	0.07
M	3	3	3259	205	0.07
M	3	4	2845	173	0.07
M	3	5	3146	196	0.08
M	3	6	3460	205	0.08
M	3	7	2604	164	0.08
M	3	8	3123	183	0.08
M	5	1	2947	192	0.08
M	5	2	2765	175	0.07
M	5	3	2211	140	0.09
M	5	4	2514	172	0.08
M	5	5	2759	185	0.08
M	5	6	3209	190	0.07
M	5	7	2868	179	0.08
M	5	8	3166	181	0.07

imum value of UCS and Young modulus were associated with the largest morphometric values. In particular, the trend of variation of these properties followed the mean strut measure. The cell also showed the highest effect of processing conditions with a difference between the minimum and the maximum values of almost 60% for *E* and 50% for UCS (Table 3).

- Cell M3 showed the highest Young modulus when produced using NET2 or NET6, while the minimum was found for NET 7. The UCS had the same trend. In this case, the significant contribution to the mechanical properties' variation was that of the stress-bearing section, while the mean strut measure and the relative density

were almost constant among the NETs. This is evident considering NET 7, where the cross-section is the minimum and the mechanical properties are the lowest.

- Cell M5 showed the highest Young modulus when produced using NET9. Comparable values were obtained for NET 6 and NET8, while the minimum was detected for NET3 where, on the contrary, the strain value was maximum. Thicker mean strut measure and higher relative density were found for NET3 and NET4. The same trend was observed for the resistant section and the relative density. In correspondence with the mentioned, maxima are spotted as the lowest mechanical properties.

Overall, it is worth to notice that the optimal process parameters for each cell size corresponds to the ones generating the lower deviation between the nominal and the actual strut size.

Averagely, in the range of the investigated parameters, it appeared that the processing setting that performed better on the average regarding the Young modulus is the one in which the inner and the outer beam current are the same, and the energy is distributed with a larger focus offset value (NET6).

## 4 Conclusions

This work has investigated the effects of the processing conditions of the PBF-EB/M process on dodecahedron unit cell lattice structure. Different cell and nominal strut dimensions fabricated under different process sets have been examined. X-ray CT scan and SEM analyses were used to investigate how the process parameters affect the actual morphometry in terms of strut diameter, node stress-bearing section and relative density, compared to the nominal dimensions. Finally, the as-built cell morphology has been correlated to the mechanical properties under compression loads.

The main findings of the work can be resumed as follows:

- Different levels of process parameters systematically affect the lattice structure morphometry and dimensional accuracy, and therefore the mechanical properties. Unexpectedly, the only variation the process parameters in small range can affect the mechanical properties by 30%.
- The effects of the process parameters on structures T3, T5 and M5 are aligned for all the analysed combinations; Structure M3 is differently affected from the process setups that let emerge the cell size effect.
- The beam current is the leading factor in the strut size determination. When increased to 3.2 mA, at the outer contour, it results in systematically thicker struts in all cases.
- A simultaneous variation of the beam current and focus offset is related to the beam diameter and, consequently, to the strut dimension.

- The focus offset level at 0 mA on the outer contour, when combined with the 2.8 mA beam current, produces thicker and more irregular struts, as observed from the deviation associated with the mean strut measure.
- The variation of the scan speed level at the inner and outer contour does not induce a systematic effect on the structures, confirming that it is not a leading factor for the determination of lattice structures geometry.
- The melt pool geometry is relevant in the conformation of the surface-breaking defects.
- The UCS and Young modulus variations follow the relative density variation for large and stocky struts (bulky beam behaviour); for thin and slender struts, the UCS and Young modulus values follow the strut dimension variation (slender beam behaviour).

Overall, the outcomes showed a significant effect of the considered lattice structure and process setup on the morphometric parameters. The analysis revealed that when the

nominally designed features are below the process resolution (technological limit), certain combinations of process parameters produced strut features hugely far from the designed one. When the technological limit is achieved, the strut size is less sensitive to the process parameter variation. Above the process resolution, even smaller variations of the processing parameters caused significant effects on the mechanical properties of the structure. When the processing condition generates a structure with low deviation from the nominal designed, this is beneficial also for the mechanical properties. As these findings are valid for all materials, the process optimisation for thin structures becomes particularly challenging. As of now, there is limited literature on the link between mechanical properties and the comparison between nominal and actual morphometric parameters and limit of the manufacturing process for each material. Therefore, extensive tests should be performed to fill that knowledge gap and accelerate the success of the design and application of lattice structures, in particular for new materials in AM portfolio, such as Ti6242.

## Appendix

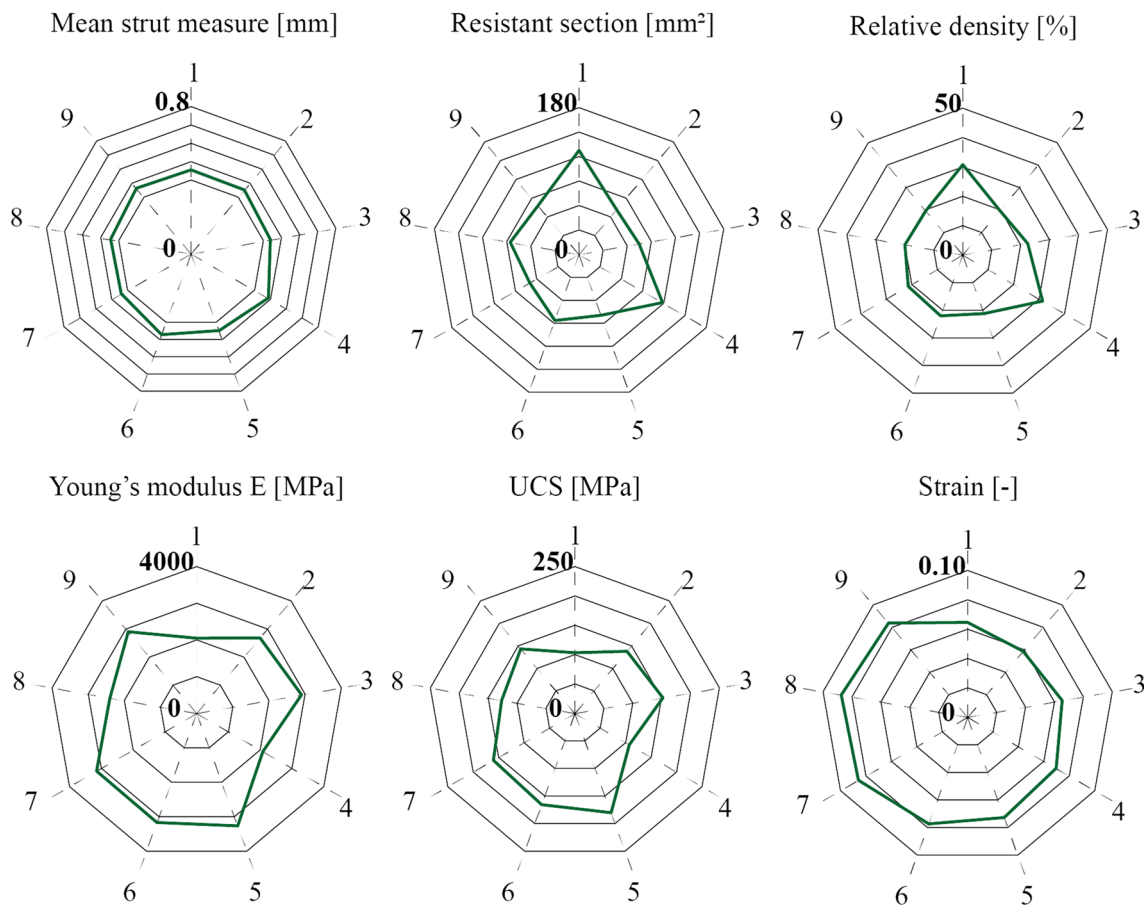


**Fig. 14** Mechanical characterisation and correlation with morphometric properties for structure T3

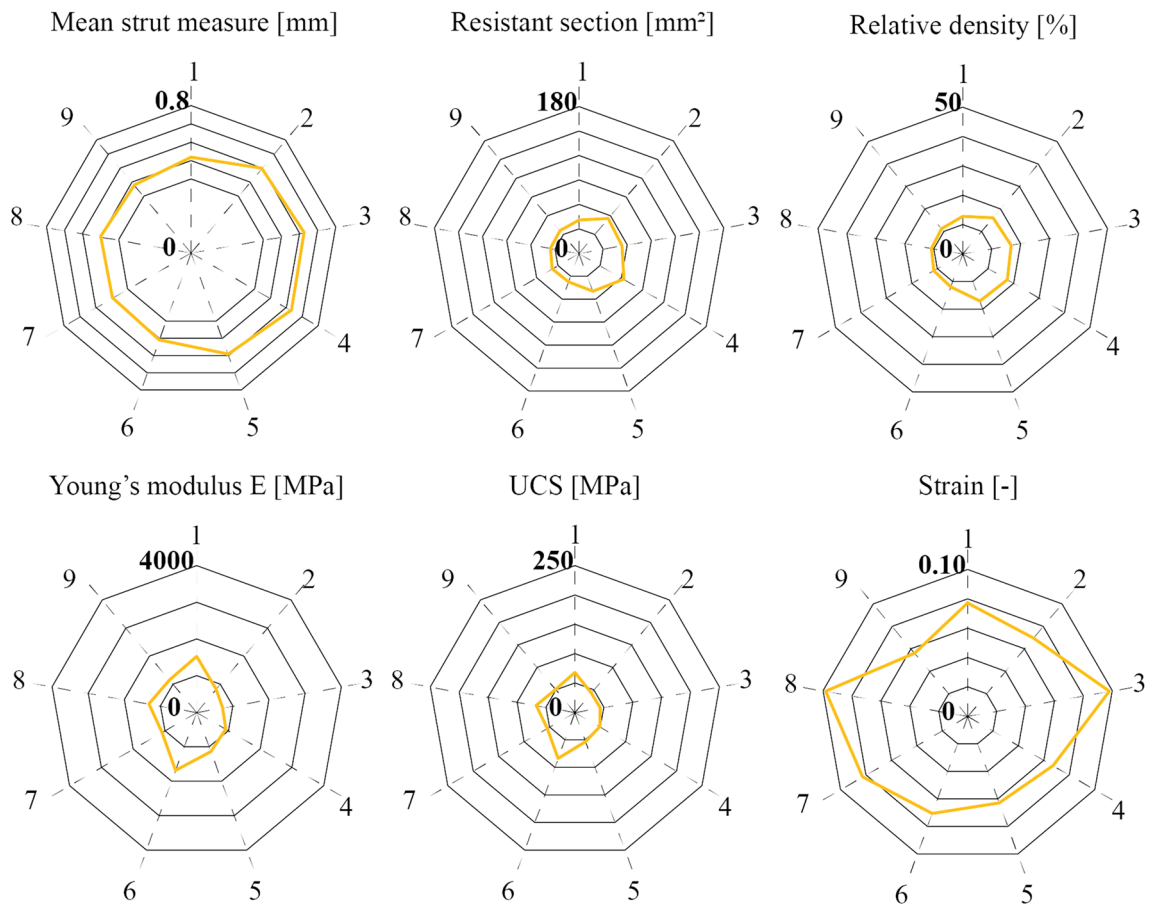


**Fig. 15** Mechanical characterisation and correlation with morphometric properties for structure T5

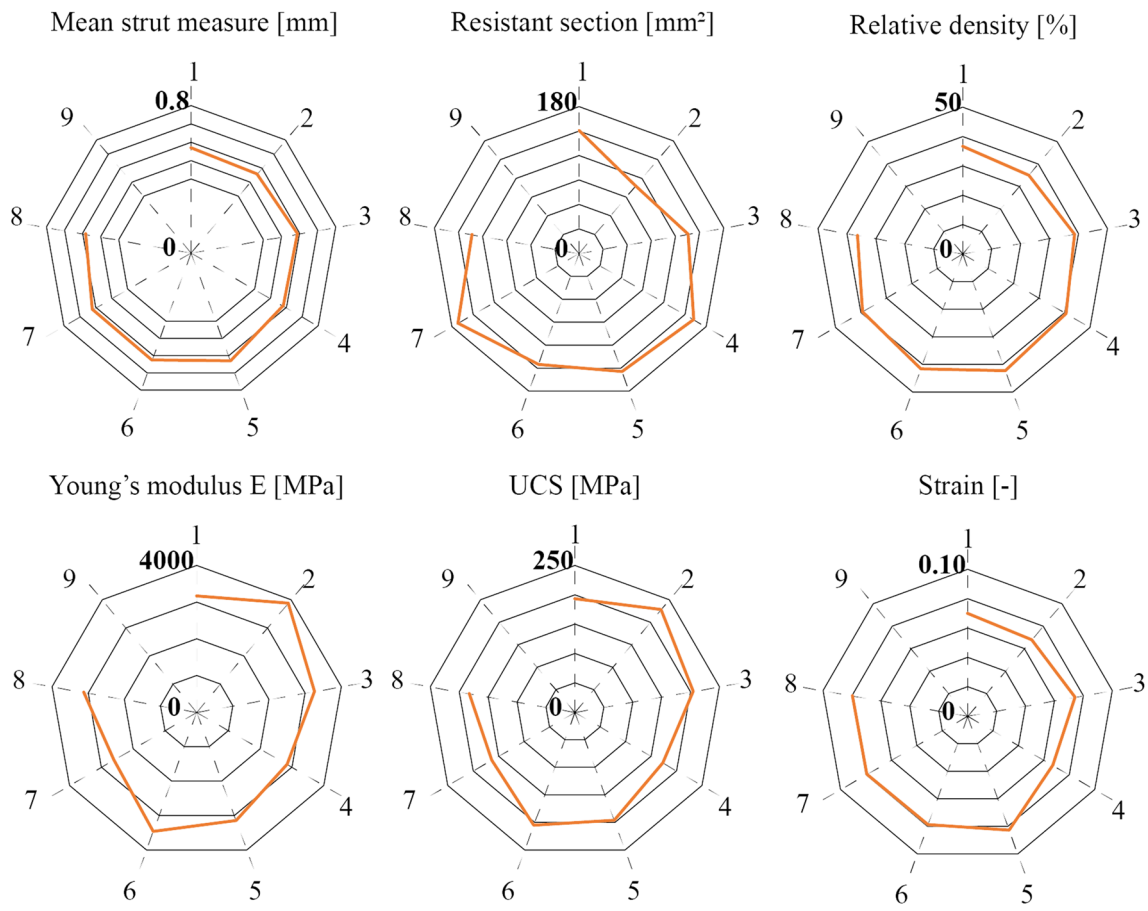
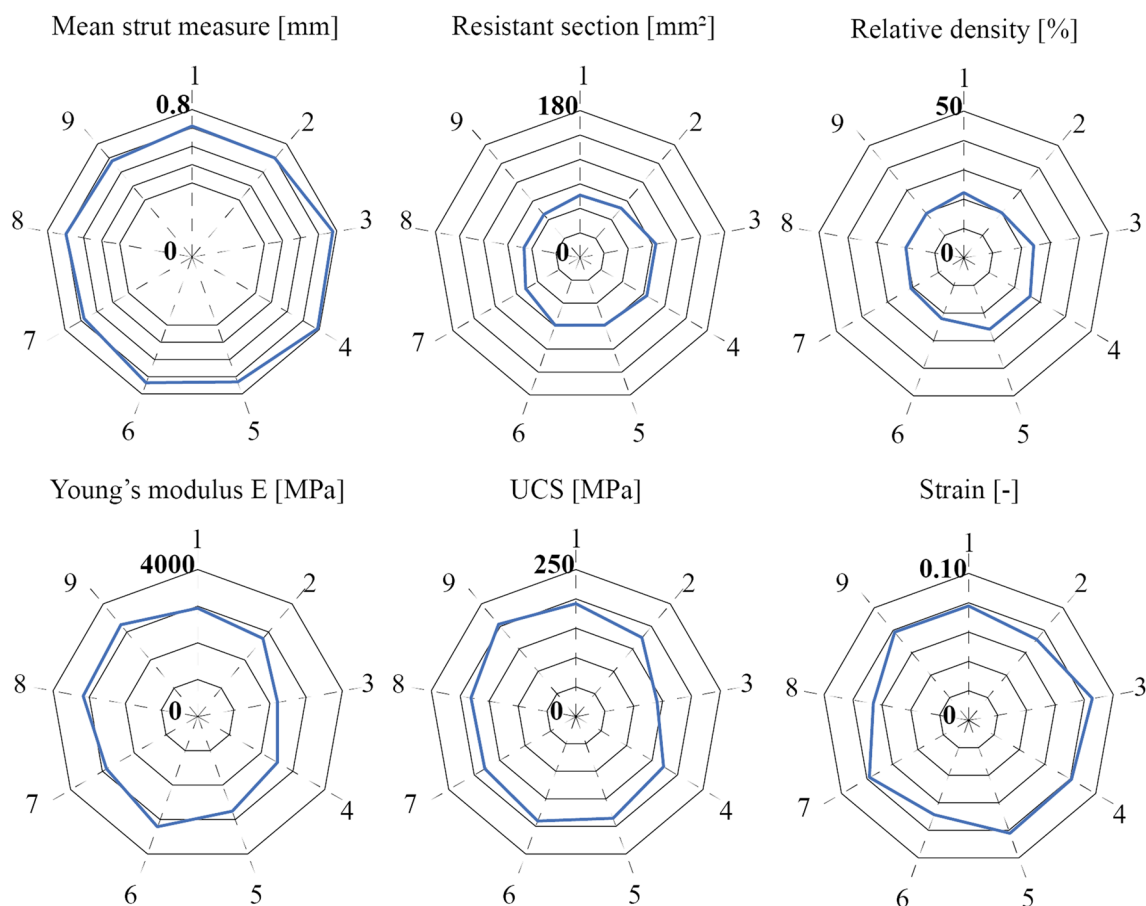


Fig. 16 Mechanical characterisation and correlation with morphometric properties for structure M3



**Fig. 17** Mechanical characterisation and correlation with morphometric properties for structure M5

**Author contributions** The study was conceived and designed by Manuela Galati. Material preparation, data collection and analysis were performed by Manuela Galati, Massimo Giordano, and Silvio Defanti. The first draft of the manuscript was written by Massimo Giordano, and all authors commented on previous versions of the manuscript. Manuela Galati and Abdollah Saboori reviewed and edited the final version of the manuscript. All authors read and approved the final manuscript.

**Funding** Open access funding provided by Politecnico di Torino within the CRUI-CARE Agreement.

## Declarations

**Competing interests** The authors declare no competing interests.

**Open Access** This article is licensed under a Creative Commons Attribution 4.0 International License, which permits use, sharing, adaptation, distribution and reproduction in any medium or format, as long as you give appropriate credit to the original author(s) and the source, provide a link to the Creative Commons licence, and indicate if changes were made. The images or other third party material in this article are included in the article's Creative Commons licence, unless indicated otherwise in a credit line to the material. If material is not included in the article's Creative Commons licence and your intended use is not permitted by statutory regulation or exceeds the permitted use, you will

need to obtain permission directly from the copyright holder. To view a copy of this licence, visit <http://creativecommons.org/licenses/by/4.0/>.

## References

1. Suard M, Martin G, Lhuissier P et al (2015) Mechanical equivalent diameter of single struts for the stiffness prediction of lattice structures produced by Electron Beam Melting. *Addit Manuf* 8:124–131. <https://doi.org/10.1016/j.addma.2015.10.002>
2. Nagesha BK, Dhinakaran V, Varsha Shree M et al (2020) Review on characterization and impacts of the lattice structure in additive manufacturing. *Mater Today: Proc* 21:916–919
3. Pan C, Han Y, Lu J (2020) Design and optimization of lattice structures : a review
4. Galati M, Giordano M, Iuliano L (2022) Process-aware optimisation of lattice structure by electron beam powder bed fusion. *Prog Addit Manuf*. <https://doi.org/10.1007/s40964-022-00339-x>
5. Kandasamy MK, Ganesan A, Srinivasan L (2022) Influence of relative density and strain rate on mechanical behavior and energy absorption of additively manufactured lattice structure. *Trans Indian Inst Met*:1–6. <https://doi.org/10.1007/s12666-022-02780-6>
6. Platek P, Sienkiewicz J, Janiszewski J, Jiang F (2020) Investigations on mechanical properties of lattice structures with different values of relative density made from 316L by selective laser



- melting (SLM). *Materials* (Basel) 13. <https://doi.org/10.3390/ma13092204>
7. Alaña M, Cutolo A, Ruiz de Galarreta S, Van Hooreweder B (2021) Influence of relative density on quasi-static and fatigue failure of lattice structures in Ti6Al4V produced by laser powder bed fusion. *Sci Rep* 11:1–15. <https://doi.org/10.1038/s41598-021-98631-3>
  8. Mahbod M, Asgari M, Mittelstedt C (2020) Architected functionally graded porous lattice structures for optimized elastic-plastic behavior. *Proc Inst Mech Eng Part L J Mater Des Appl* 234:1099–1116. <https://doi.org/10.1177/1464420720923004>
  9. Park JW, Park H, Kim JH et al (2022) Fabrication of a lattice structure with periodic open pores through three-dimensional printing for bone ingrowth. *Sci Rep* 12:1–8. <https://doi.org/10.1038/s41598-022-22292-z>
  10. Cheng XY, Li SJ, Murr LE et al (2012) Compression deformation behavior of Ti–6Al–4V alloy with cellular structures fabricated by electron beam melting. *J Mech Behav Biomed Mater* 16:153–162. <https://doi.org/10.1016/j.jmbbm.2012.10.005>
  11. Hussein A, Hao L, Yan C et al (2013) Advanced lattice support structures for metal additive manufacturing. *J Mater Process Technol* 213:1019–1026. <https://doi.org/10.1016/j.jmatprotec.2013.01.020>
  12. Körner C (2016) Additive manufacturing of metallic components by selective electron beam melting—a review. *Int Mater Rev*:1–17
  13. Galati M (2021) Electron beam melting process. In: *Additive manufacturing*. Elsevier, pp 277–301
  14. Siemers C, Bäker M, Brunke F et al (2018) Aluminum- and vanadium-free titanium alloys for application in medical engineering. In: *Titanium in medical and dental applications*. Woodhead Publishing
  15. Gogia AK (2005) High-temperature titanium alloys. *Def Sci J* 55:149–173. [10.14429/dsj.55.1979](https://doi.org/10.14429/dsj.55.1979)
  16. Galati M, Defanti S, Saboori A et al (2022) An investigation on the processing conditions of Ti-6Al-2Sn-4Zr-2Mo by electron beam powder bed fusion: microstructure, defect distribution, mechanical properties and dimensional accuracy. *Addit Manuf* 50. <https://doi.org/10.1016/j.addma.2021.102564>
  17. Del Guercio G, Galati M, Saboori A (2021) Electron beam melting of Ti-6Al-4V lattice structures: correlation between post heat treatment and mechanical properties. *Int J Adv Manuf Technol* 116:3535–3547. <https://doi.org/10.1007/s00170-021-07619-w>
  18. Teimouri M, Mahbod M, Asgari M (2021) Topology-optimized hybrid solid-lattice structures for efficient mechanical performance. *Structures* 29:549–560. <https://doi.org/10.1016/j.istruc.2020.11.055>
  19. Tamas-Williams S, Zhao H, Leonard F et al (2015) XCT analysis of the influence of melt strategies on defect population in Ti-6Al-4V components manufactured by Selective Electron Beam Melting. *Mater Charact* 102:47–61. <https://doi.org/10.1016/j.matchar.2015.02.008>
  20. Galati M, Snis A, Iuliano L (2018) Experimental validation of a numerical thermal model of the EBM process for Ti6Al4V. *Comput Math with Appl* 78:2417–2427. <https://doi.org/10.1016/j.camwa.2018.07.020>
  21. Xiao L, Li S, Song W et al (2020) Process-induced geometric defect sensitivity of Ti–6Al–4V lattice structures with different mesoscopic topologies fabricated by electron beam melting. *Mater Sci Eng A* 778:139092. <https://doi.org/10.1016/j.msea.2020.139092>
  22. Galati M, Rizza G, Defanti S, Denti L (2021) Surface roughness prediction model for electron beam melting (EBM) processing Ti6Al4V. *Precis Eng* 69. <https://doi.org/10.1016/j.precisioneng.2021.01.002>
  23. Bassoli E, Mantovani S, Giacalone M et al (2023) On the technological feasibility of additively manufactured self-supporting AlSi10Mg lattice structures. *Adv Eng Mater* 25:2201074. <https://doi.org/10.1002/adem.202201074>
  24. Mantovani S, Giacalone M, Merulla A et al (2021) Effective mechanical properties of AlSi7Mg additively manufactured cubic lattice structures. *3D Print Addit Manuf* 9(4):326–336. <https://doi.org/10.1089/3dp.2021.0176>

**Publisher's Note** Springer Nature remains neutral with regard to jurisdictional claims in published maps and institutional affiliations.